

Nanoscale

Accepted Manuscript



This is an *Accepted Manuscript*, which has been through the Royal Society of Chemistry peer review process and has been accepted for publication.

Accepted Manuscripts are published online shortly after acceptance, before technical editing, formatting and proof reading. Using this free service, authors can make their results available to the community, in citable form, before we publish the edited article. We will replace this *Accepted Manuscript* with the edited and formatted *Advance Article* as soon as it is available.

You can find more information about *Accepted Manuscripts* in the [Information for Authors](#).

Please note that technical editing may introduce minor changes to the text and/or graphics, which may alter content. The journal's standard [Terms & Conditions](#) and the [Ethical guidelines](#) still apply. In no event shall the Royal Society of Chemistry be held responsible for any errors or omissions in this *Accepted Manuscript* or any consequences arising from the use of any information it contains.

ARTICLE

Metallic Nanowire Networks: Effects of Thermal Annealing on Electrical Resistance

Cite this: DOI: 10.1039/x0xx00000x

D. P. Langley^{a,b}, M. Lagrange^a, G. Giusti^a, C. Jiménez^a, Y. Bréchet^c, N. D. Nguyen^b and D. Bellet^a,Received 00th January 2012,
Accepted 00th January 2012

DOI: 10.1039/x0xx00000x

www.rsc.org/

Metallic nanowire networks have huge potential in devices requiring transparent electrodes. This article describes how the electrical resistance of metal nanowire networks evolve under thermal annealing. Understanding the behavior of such films is crucial for the optimization of transparent conductive electrodes which find many applications. An in-depth investigation of silver nanowire networks under different annealing conditions provides a case study demonstrating that several mechanisms, namely local sintering and desorption of organic residues, are responsible for the reduction of the systems electrical resistance. Optimization of the annealing led to specimens with transmittance of 90 % (at 550 nm) and sheet resistance of 9.5 Ω /sq. Quantized steps in resistance were observed and a model is proposed which provides good agreement with the experimental results. In terms of thermal behavior, we demonstrate that there is a maximum thermal budget that these electrodes can tolerate due to spheroidization of the nanowires. This budget is determined by two main factors: the thermal loading and the wire diameter. This result enables the fabrication and optimization of transparent metal nanowire electrodes for solar cells, organic electronics and flexible displays.

1. Introduction

Metallic nanowires (NWs) have recently received increasing interest due to their potential application as interconnects and as essential components in nanoelectronics.¹ Metallic NW networks are also promising candidates to be used as transparent conductive material for many industrial purposes. Their physical and chemical properties differ from the properties of the bulk material and are strongly related to both the size and structure of the NWs themselves. When used as a network, their characteristics, such as wire diameter, density of wires in the network and junction resistance, have a significant impact on the physical properties of the whole.²

When working with metallic nanowires for transparent electrode applications the main goal is to obtain an electrode which has the lowest electrical conductivity for a given optical transmission.

Optimizing the electrical resistance and optical transmission of

nanowire networks involves tuning several key parameters including the experimental conditions of deposition, wire geometry,³ network density and post-deposition treatments such as mechanical pressing,⁴ light-induced plasmonic nanowelding^{5–7} or thermal annealing.^{8–10} All of these post-deposition treatments have been shown to decrease the electrical resistance. However, thermal annealing has not yet been the subject of a detailed investigation. The impact of thermal annealing on the electrical resistance of metallic NW networks is dominated by desorption of organic residues and local sintering at the junction between neighbouring nanowires,^{8,10–12} both of which lead to a significantly lower contact resistance. This is a clear asset of metallic NW network when compared with carbon nanotubes which suffer from high junction resistance between nanotubes.¹³

Although thermal annealing can lower the electrical resistance of metallic nanowire networks, instability of the nanowires upon an excessive heating results in a critical limit of the thermal budget applied on the system, which requires dedicated analysis.¹⁴ Cylindrical metallic nanowires are known to be energetically unstable and can fragment at temperatures significantly lower than their melting point.^{15–18} This is the result of a morphological instability, called the Rayleigh instability, and is a critical issue for the long-term reliability of micro- and nano-electronic devices. These thermal instabilities

^a Univ. Grenoble Alpes, LMGP, F-38000 Grenoble, France
CNRS, LMGP, F-38000 Grenoble, France.

^b Laboratoire de Physique des Solides, Interfaces et Nanostructures; Département de Physique, Université de Liège. Allée du 6 Août 17, B-4000 Liège, Belgium.

^c Univ. Grenoble Alpes, SIMAP, F-38000 Grenoble, France
CNRS, SIMAP, 1130 rue de la Piscine -F-38402 St Martin D'Heres

place limitations on the thermal budget that an electrode may undergo during device fabrication. For example the use of metal NW electrodes in TiO₂

Dye Sensitized Solar Cells (DSSCs) may be restricted due to the need to sinter the TiO₂ nanoparticle layers for 1 hour at 450 °C.^{19,20} It has been suggested recently that a second instability may also be observed due to Joule heating when metallic nanowire networks are used with current densities similar to those found in a solar cell of ≈10% efficiency, leading to electrode failure in a matter of days.²¹ Such instabilities and the mechanisms leading to them need to be understood to enable the efficient integration of metallic NW networks in real devices.

Due to their promising electrical and optical properties, silver nanowires (AgNWs) have been intensively investigated for use as a transparent conductive material.^{2,5,22–24} Such networks have been applied to several different types of devices, including: solar cells,^{25,26} flexible light-emitting devices and displays,²⁷ stretchable electrodes²⁸ and flexible transparent thin film heaters.^{29,30}

In this work, we studied the effects of thermal annealing on the electrical properties of AgNW networks. The main goal is to better understand their behaviour and to optimize the electrical properties of the annealed network. Since several physical mechanisms are at play, different types of annealing have been employed (isothermal, thermal ramps and pre-annealing) in order to disentangle the possible causes responsible for the variations of the electrical resistance observed in-situ.

2. Results

2.1 THERMAL ANNEALING

The most direct way to probe the effect of thermal annealing on the electrical resistance of AgNWs is to measure their resistance *in-situ* during a thermal ramp in air. The evolution of the electrical resistance of an AgNW network versus temperature during a thermal ramp at 15 °C/min in air is shown in Figure 1 a). The electrical resistance varies by several orders of magnitude and clearly exhibits a minimum. Several mechanisms are responsible for the observed variations in resistance as a function of temperature.

This type of annealing, with $T(t) = T_0 + \dot{T} \cdot t$, where $T(t)$ is the temperature at time t , T_0 is the initial temperature and \dot{T} is the heating rate, is classically used for the quantitative determination of the desorption activation energy.³¹ At low temperatures (50-125 °C) several sudden drops of resistance $R(t,T)$ can be observed in Figure 1a and 1f (both within the highlighted frames) and will be discussed in detail below. In Figure 1b a SEM image of an as-deposited nanowire network is displayed. It can be seen that the nanowires are coated with a carbonaceous shell which is approximately 30 nm thick. This shell is a combination of polyvinylpyrrolidone (PVP) from the nanowire synthesis³² and organic residues from the solution based deposition. The removal of these organic contaminants and/or residual isopropyl alcohol (IPA) decreases the electrical resistance of the contact between NWs. The reduced resistance

leads to the formation of efficient conduction pathways through the network.

At higher temperatures (125-170 °C) $R(t,T)$ continues to decrease with increasing temperature and becomes a continuous

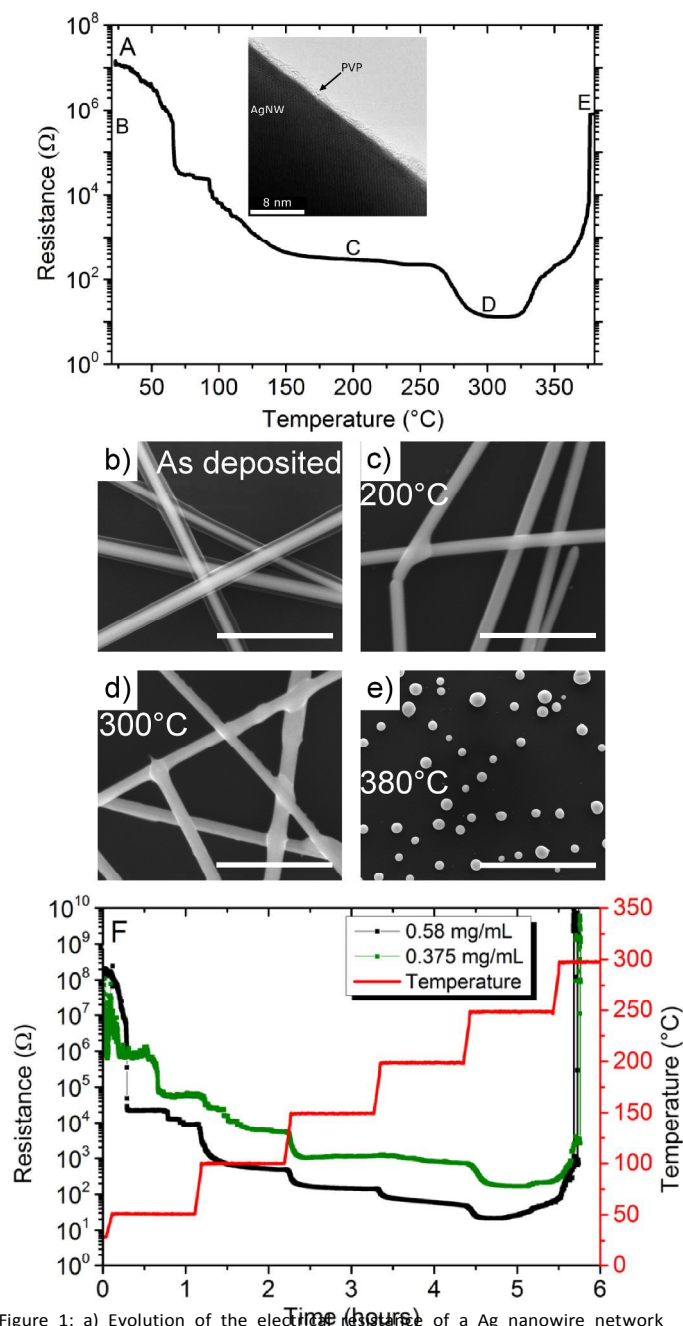


Figure 1: a) Evolution of the electrical resistance of a silver nanowire network during a continuous thermal ramp of 15 °C/min from room temperature (associated with deposition solution of 0.75 mg/mL and an areal mass density of ≈105 mg/m²). The inset image is a TEM micrograph of a silver nanowire showing residual PVP from synthesis. b-e) Scanning electron microscope (SEM) images of: b) as-deposited sample and of specimen annealed for 10 minutes at different temperatures: c) 200 °C, first occurrence of observable sintering; d) 300 °C all junctions are sintered; e) 380 °C complete spheroidization of the network. Image e) is at a lower magnification than the others to demonstrate that although the nanowires are completely spheroidized the resultant nanoparticles are still aligned at the original position of the wires. The scale bars in images b), c) and d) are 1 μm whereas that of image e) is 4 μm. f) Resistance response of two

specimens to a series of increasing isothermal anneals (associated with deposition solutions of 0.58 mg/mL and 0.375 mg/mL resulting in areal mass densities of $\approx 81 \text{ mg/m}^2$ and $\approx 53 \text{ mg/m}^2$, respectively). All data shown in Figure 1 were obtained using AgNW for which average wire diameter was 105 nm and average wire length was 37.3 μm .

process which resembles an exponential decay. This can be assigned to the continued desorption of organic residues and the polymer coating (PVP) from the AgNWs. Figure 1c exhibits a SEM image of a specimen annealed at 200 °C for 10 minutes: it is clearly visible that the majority of the carbonaceous film has been removed, however the thin film ($\sim 2.5 \text{ nm}$ see Figure 1a inset) of PVP remains on the surface. At $\approx 170 \text{ °C}$ the rate of reduction in $R(t, T)$ slows down as the desorption of organic components tails off due to the decreased concentration of remaining isopropanol and other organic residues. Above 200 °C local sintering begins at NW junctions, as revealed by the SEM picture shown in Figure 1c. The rate of sintering is slow at first due to remaining PVP, thermo gravimetric analysis revealed that there is an exothermic reaction occurring between 250 °C and 270 °C. This result is similar to that found previously by Lee et al.¹² and was assigned to the degradation of PVP. Above 270 °C sintering occurs more rapidly resulting in a continued drop in resistance. Again, this takes the form of an exponential function. For this temperature range, as the population of unsintered junctions decreases the rate of junction sintering decreases. A minimum in $R(t, T)$ is observed from 300–320 °C. For higher temperatures $R(t, T)$ increases sharply. This is attributed to the onset of a morphological instability which results in spheroidization of the nanowires as observed in SEM image of Figure 1e. While thermal annealing has a significant impact on the electrical resistance of AgNW networks (with decrease of several orders of magnitude) the optical transmittance remains identical within experimental errors.

Since electrical properties for a given thermal equilibrium state and kinetic effects are intertwined, it is difficult to determine the exact temperature ranges over which the above-mentioned stages occur from the results shown in Figure 1a (temperature ramp). However, observation of Figure 1a–e leads to a general trend of the effect of temperature on silver nanowire networks, which can be described by three main stages:

Reduction: Initially the resistance drops as the residual solvents and PVP are removed from the network. A second reduction phase is observed due to the onset of local sintering at the junctions.

Stabilisation: As the number of unsintered junctions decreases the electrical resistance reduction rate slows down and the resistance value stabilizes briefly, this is associated with the minimum resistance.

Spheroidisation: Morphological instabilities of the nanowires occur and the resistance increases rapidly as the NW network degrades into separated spheres and loses its percolative nature.

Experiments with in-situ monitoring of the resistance variation using a thermal ramp provide a nice overview of the thermal annealing effects. However, during a thermal ramp multiple

processes may occur simultaneously as they have not had enough time to reach completion before a second mechanism starts. One method to shed light on the thermal annealing effects is thus to consider isothermal annealing with plateaus at various temperatures, as reported in Figure 1f. The same 3 stages seen in Figure 1a are observed for the isothermal stepped annealing process depicted in Figure 1f. Due to the separation of kinetics and activation temperature the mechanisms at play occur at different temperature ranges compared to the ramped annealing shown in Figure 1a.

Figure 1f also exhibits sharp drops in the specimen resistance at low temperature ($\leq 100 \text{ °C}$) again a detailed discussion of this behavior is provided in section 2.2. At 100 °C and above, $R(t, T)$ exhibits an initial rapid decrease for each temperature plateau lower than 250 °C. At 250 °C the resistance plateaus and for a period of several minutes remains constant before R increases due to the onset of the morphological instability of the AgNWs. This then gives indication of both the optimized temperature where the electrical resistance of the network can be minimized through balancing the sintering effects and thermal stability of the AgNWs. The denser network exhibits a lower electrical resistance as a result of the increased number of conduction pathways and at the expense of a lower optical transparency. The network density results in a tradeoff between high optical transparency (obtained for sparse networks) and efficient electrical conductivity (associated with a high NW density).²²

2.2 QUANTIZED ACTIVATION OF PERCOLATION

The drops of electrical resistance observed in both Figure 1a and 1f can be understood in the following way; they correspond to the creation of the first efficient pathways through the network composed of AgNW and junctions between them. The junction resistances are high before thermal annealing and decrease as a function of time when the temperature is increased, as shown by Figure 1a and 1f. For all specimens studied the resistance drops occur at a resistance of several thousands of ohms, which is of the same order of magnitude as the resistance of a long hypothetical NW crossing the whole network. This estimate is based on Ohm's law applied on an efficient percolating path (EPP) which is a cylinder of length L (in this case the width of the whole network $\approx 7 \text{ mm}$ long), cross-sectional area S and electrical resistivity ρ . The associated electrical resistance R_{EPP} can be written as:

$$R_{EPP} = \frac{K\rho L}{S} \quad (1)$$

where K is a constant associated with the actual path length of the percolating path (which is longer than the network width due to the tortuous nature of percolating paths as schematically shown by Figure 2a), and therefore on the density of the network, as well as the electrical resistance of the junctions which act as series resistances along the conduction pathway. Therefore, K is expected to be larger than one.

The validity of using silver bulk resistivity ($1.59 \times 10^{-8} \Omega\text{m}$) for nanowires of this size is questionable as the wire diameter is

approaching the mean free path of electrons in bulk silver. The reduced diameter results in a significant increase in the impact of surface scattering on the resistivity of the wires. It has been demonstrated that the resistivity of nanowires is dependent on the wire diameter and increases above that of the bulk significantly.³³ In the case of AgNWs with a diameter 100nm, Bid *et al.* found the resistivity to be $2.78 \times 10^{-8} \Omega\text{m}$.³³ Considering the NW diameter (105 nm on average), R_{EPP} is on the order of a few thousand ohms, in good agreement with the steps in resistance observed at low temperature in Figure 1a and 1f. This first efficient percolating pathway (EPP) (represented schematically in Figure 2a by thicker red NWs) exhibits an electrical resistance, named R_{EPP} , which should contribute in parallel to the resistance of the initial network, noted R_S .

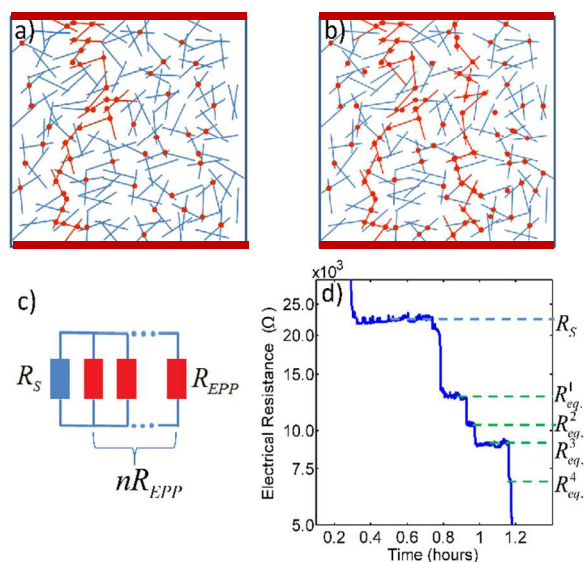


Figure 2: a) Schematic representation of a NW network; under thermal annealing, some of the junctions become efficient (indicated by red dots). When a sufficient number of junctions are activated, an efficient percolating pathway forms between the top and bottom electrodes. b) As heating continues, additional efficient pathways form. c) The pathways can be considered as n resistances R_{EPP} in parallel with an initial system resistance R_S . d) Experimental data exhibiting plateaus in resistance which can be assigned as equivalent resistances R_{eq}^n which are the parallel sum of R_S and n resistances R_{EPP} , where n is an integer which increases as thermal annealing proceeds.

A second EPP appears slightly later, as shown in Figure 2b) and again acts as an additional parallel resistance R_{EPP} , which leads to another drop of R as shown experimental by Figure 1a and 1f. Therefore the simplest model defines the electrical resistance of the network after the n^{th} resistance drop as the equivalent resistance consisting of R_S in parallel with n electrical resistances R_{EPP} (as shown in Figure 2.c), leading to the following expression:

$$\frac{1}{R_{eq}^n} = \frac{1}{R_S} + \frac{n}{R_{EPP}} \quad (2)$$

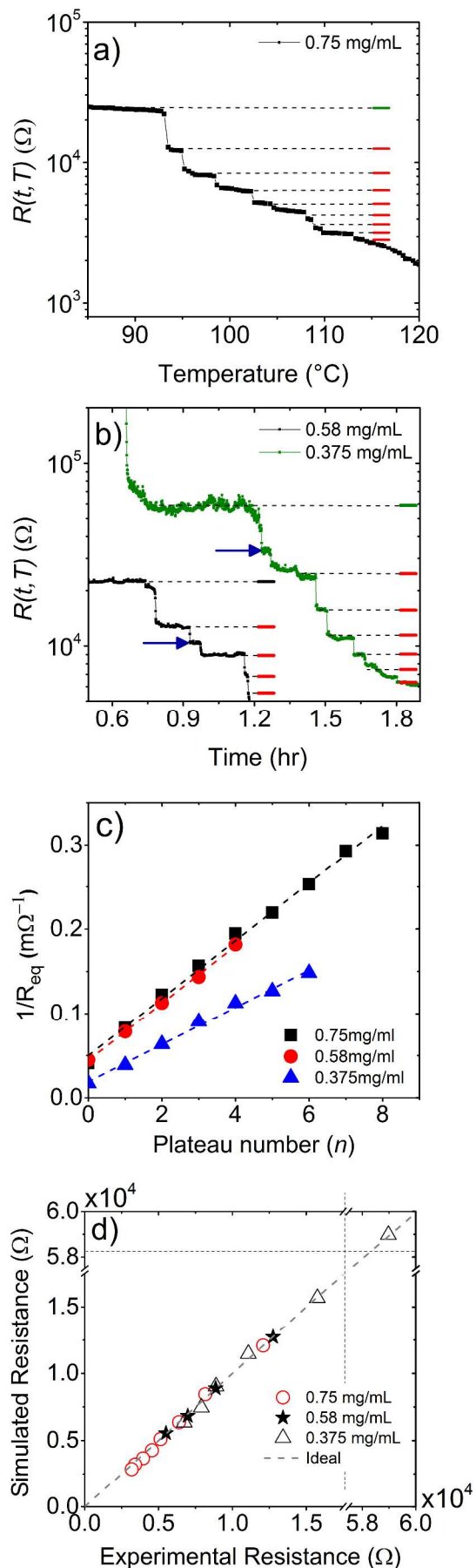
The experimental values of R_{eq} are schematically shown on Figure 2 d). R_S can be defined by the experimental resistance before the appearance of the first drop. R_{EPP} can be determined

by equation 1 where all parameters are known except K which remains the only fitting parameter of the model and is kept constant for all resistance drops observed on a given specimen. The regions which exhibit steps in the resistance from Figure 1a and 1f are enlarged and compared in Figure 3a and 3b to the values calculated by fitting K using equation 1 and 2 (shown as solid lines to the right of the experimental data).

Despite the simplicity of the model, the agreement between the experimental data and the calculated values is excellent. From Figure 3c) it is clear that the resistance is described well by equation 2 and that the fitting parameter K for equation 1 can be calculated. R_S and R_{EPP} values were determined from a linear fit of the experimental data (see Figure 3c) according to equation 2. The R_S values obtained from these fits correspond well to those observed experimentally, while R_{EPP} values are larger than $\rho L/S$ in agreement with equation 1. The latter enables calculation of the K values which are 1.15, 1.31 and 1.91 for specimens associated with solution concentration of 0.75, 0.58 and 0.375 mg/mL, respectively.

In Figure 3d) a comparison is given between experimental data and values calculated with equation 1 and equation 2, showing excellent agreement with a K value varying between 1.15 and 1.91 as the network density decreases. It is not surprising that the value of K increases as the density of the network decreases, as K is a proportionality factor relating to the actual length of the individual conduction pathways. In a dense network there are many more junctions per unit area and the probability of finding a direct path is much higher. As the network density decreases the path becomes more tortuous thus increasing the effective distance between electrodes, and hence the value of K . As with all models there are simplifications that must be made, the proposed model assumes that all pathways are independent and electrically connected in parallel. In reality the system can be more complicated and partial pathways and series connections between pathways may also appear (a schematic way to imagine such a pathway is to consider a Y shape for the partial pathways and a H shape for the series connections between paths). Examples can be seen in Figure 3 b) where the plateaus indicated by blue arrows do not match a calculated data point, these plateaus are considered as partial pathways connecting to one of the existing efficient conductive paths.

Initially when the number of efficient junctions is low the probability of observing the formation of a new EPP is low. As annealing continues more junctions are sintered and the chance to form an EPP increases. After the formation of the first efficient percolating path it is expected that the efficient junction density is sufficiently high that other pathways also begin to form in a more and more rapid succession. When plotted in the time domain (Figure 3b) this should be seen as the length of plateaus decreasing on average as the number of plateaus increases. However this is a statistical process so the length of the plateaus are somewhat random, hence the experimental variability of the plateau length. As the number of EPP increases it becomes increasingly likely that new efficient paths overlap with existing paths, thus as n increases so too does the probability of partial path formation, this results in the



loss of quantized steps in $R(t, T)$ as the number of plateaus

This journal is part of the Nanoscale journal series.

increases and a continuous drop in resistance is eventually observed (typically for values lower than 1000 Ω) for long annealing or at higher temperature.

R_{eq}^n Initially when the number of efficient junctions is low the probability of observing the formation of a new EPP is low. As

Figure 3: a) and b) Experimental electrical resistance drops observed during thermal annealing (continuous line) for samples of different densities and comparison with the proposed model (dashed lines). Data shown in a) corresponds to the highlighted section of Figure 1a (i.e. during a thermal ramp) while data in b) corresponds to the highlighted section of Figure 1f (along a temperature plateau). Arrows in the plot indicate plateaus which were identified as partial percolating pathways. c) Plot of $1/R_{eq}$ as a function of plateau number n extracted from the experimental plateaus of the curves in Figure 3a and 3b (dashed lines are a linear fit based on equation 2) d) Comparison of the predicted values to experimental electrical resistances, the dashed line represents a slope of one indicating a perfect correlation. The used K values were 1.15, 1.31 and 1.91 associated with deposited solution concentration of 0.75, 0.58 and 0.375 mg/mL, respectively.

annealing continues more junctions are sintered and the chance to form an EPP increases. After the formation of the first efficient percolating path it is expected that the efficient junction density is sufficiently high that other pathways also begin to form in a more and more rapid succession. When plotted in the time domain (Figure 3b) this should be seen as the length of plateaus decreasing on average as the number of plateaus increases. However this is a statistical process so the length of the plateaus are somewhat random, hence the experimental variability of the plateau length. As the number of EPP increases it becomes increasingly likely that new efficient paths overlap with existing paths, thus as n increases so too does the probability of partial path formation, this results in the loss of quantized steps in $R(t, T)$ as the number of plateaus increases and a continuous drop in resistance is eventually observed (typically for values lower than 1000 Ω) for long annealing or at higher temperature.

Let us finally consider that while stick percolation is generally a density problem, in the present case the model works at a constant stick density upon which a network of junction resistances is applied which play the role of the percolation sites. Each site is a given resistance which is reduced by thermal annealing; conduction through the system will occur predominantly through low resistance junctions. These junctions represent a very large population (measured experimentally as about 10^7 cm^{-2} for a specimen with similar density to that shown in Figure 1a) with a large distribution of junction resistances. In the as-deposited state the majority of the junctions have a high electrical resistance. By heating, some of these junctions become more conductive. As the annealing proceeds, clusters of nanowires are connected by efficiently conducting junctions. When a large enough number of junction resistances are reduced, an efficient percolating pathway is formed spanning the network resulting in the sudden drops of the resistance reported in Figure 3. The sudden electrical resistance drops observed in Figure 3 can therefore be considered as quantized activation of percolation.

2.3 PRE-ANNEALING

Another way of studying the effects of thermal annealing is to perform a pre-annealing at low temperature (in the present paper, a pre-annealing is considered as an isothermal anneal performed after the AgNW network fabrication and before a continuous ramp annealing). The effects of such pre-annealing on an experiment similar to the one reported in Figure 1 (i.e. thermal ramp) are shown on **Figure 4**. Pre-annealing was performed at 100 °C, 150 °C and 200 °C for 8, 6 and 2 hours, respectively. The appropriate duration of each pre-anneal was determined by monitoring in situ the resistance of the network: when the resistance became stable the pre-anneal was considered to have reached completion. This allows the exploration of temperature ranges over which different mechanisms are active.

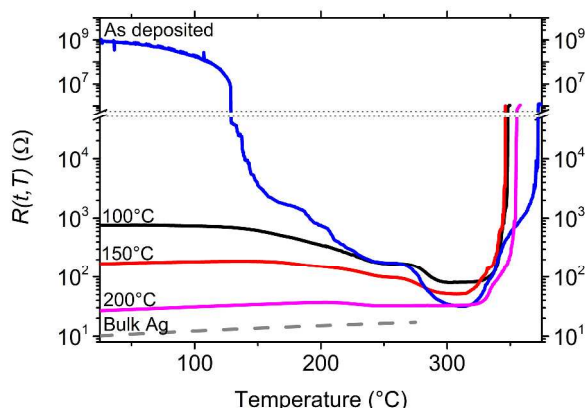


Figure 4: Temperature dependence of the electrical resistance $R(t, T)$ of silver nanowire networks (concentration of 0.75 mg/mL) during a ramp thermal annealing of 15 °C per minute for 4 different samples: as-deposited and pre-annealed at 100 °C, 150 °C and 200 °C. The dashed curve is associated with the temperature-dependence of bulk silver resistivity, showing a good agreement between experimental data and phonon-induced increase of $R(t, T)$ for the 200 °C pre-annealed specimen up to 200 °C.

The effects of the pre-annealing is drastic for the $R(t, T)$ dependence in the low temperature range (i.e. below 270 °C). There is a continuous effect of pre-annealing for which a higher associated temperature corresponds to a lower $R(t, T)$ value in the low temperature range. Then for the higher temperature range the $R(t, T)$ behavior remains similar for all specimens: the pre-annealing does not appear to influence the onset of the NW instability.

Note that for the pre-annealing at 200 °C, the increase of the $R(t, T)$ versus temperature (below 200 °C) corresponds rather well to the increase of the electrical resistivity of bulk Ag associated with the scattering of electrons by the phonon population. This corresponds to the resistivity temperature dependence:

$$\rho(T_0 + \Delta T) = \rho_0(T_0) \cdot (1 + \beta \cdot \Delta T) \quad (3)$$

where β is equal to $2.8 \times 10^{-3} \text{ K}^{-1}$ for bulk silver.³⁴ Such dependency is shown as the dashed line in Figure 4: the experimental slope of the 200 °C preannealed AgNW network is close to the one calculated with the bulk silver β value

(although such a simple calculation does not consider the junction resistances between adjacent NWs).

2.4 PHYSICAL MECHANISMS AT PLAY DURING THERMAL ANNEALING:

We discuss now the relevant physical mechanisms at play for the evolution of the networks electrical properties during thermal annealing. These mechanisms are: solvent desorption, PVP desorption, sintering at contacts between adjacent nanowires and spheroidization. The first three mechanisms act to decrease the electrical resistance of the network while the last one leads to a drastic increase of $R(t, T)$. We will discuss these four mechanisms and their impact on the experimental results presented above.

The prevailing mechanism at play at low temperature (30-140 °C) is desorption. At first, physical desorption of organic residues is responsible. Organic residues in the form of a very thin shell as visible in Figure 1b are present between AgNWs due to capillary effects and act as electrical barriers, resulting in a high electrical resistance. The physical desorption of these residues enables a more intimate contact between NWs reducing the electrical resistance. After a pre-annealing at 100 °C for 8 hours is performed, the $R(t, T)$ curve exhibits a continuous behavior (no more sudden drops are observed) and $R(t, T)$ values are much smaller, indicating that there are already a large number of efficient conduction paths through the network. At 150 °C the glass transition temperature of PVP is reached, the thin shell of PVP coating the AgNWs ($\approx 5\text{nm}$) begins to flow; this allows a more intimate contact between adjacent AgNWs, also decreasing the electrical resistance. At higher temperatures (150-250 °C) the PVP undergoes thermal degradation and is completely removed from the surface of the wires (at least in air while different behavior can be observed under vacuum³⁵). The reduction in $R(t, T)$ observed from 200-250 °C in Figure 1f originates from the onset of local sintering, as indicated by the SEM observations (see Figure 1c and d). It is important to note that for ramped annealing as shown in Figure 1a and Figure 4 this drop in $R(t, T)$ due to sintering is observed at higher temperature (275-300 °C). This difference is likely due to the kinetics of the system. As both the experiments depicted by Figure 1a and 4 are performed as thermal ramps at 15 °C/min there is insufficient time for all of the PVP and organic residues to be removed in the temperature range 200-250 °C, which results in a delay of the sintering. The preannealing shown in Figure 4 allows some separation of the kinetics and critical temperatures of various mechanisms. Comparing the $R(t, T)$ of the as deposited sample to the initial resistance of the preannealed samples reveals that for each of the preanneal treatments the initial resistance corresponds closely to a plateau in the as-deposited $R(t, T)$. These plateaus result from a kinetic pinning of the onset of different mechanisms; as the samples are exposed to a thermal ramp the temperature continues to increase before each mechanism has reached completion. By performing a preanneal until the resistance stabilizes at different temperatures we reveal what the final resistance of the network obtained is once the

mechanisms activated at the given temperature reach completion. This leads to the observation that sintering processes can reach completion at a temperature as low as 200 °C if sufficient time is provided. Sintering is the term usually used to describe the increase in mechanical strength and decrease in porosity of powder particle network when heated at a temperature approaching, but below, its melting point.^{36,37}

In the present study, as the sintering mechanism concerns only the contacts between adjacent NWs, this process is called local sintering. This corresponds to the initial stages of the usual sintering phenomenon in powder metallurgy. The associated driving force for sintering is the reduction of surface energy. In general the smaller the particle size the lower the temperature where sintering will be observed. For instance the investigation of the sintering effect on the morphology and conductivity of Ag particles of 40 nm in diameter showed that sintering occurred at 100 °C and probably even below,³⁸ while the melting point of silver is 962 °C.³⁴ In the case of AgNWs, sintering appears to be nearly complete after a pre-annealing at 200 °C for 2 hours since no further $R(t, T)$ decrease is observed as shown in Figure 4 (as compared to the specimens pre-annealed at 150 °C or below).

2.5 SPHEROIDIZATION

When submitted to a thermal annealing, nanowires can fragment into a chain of nanospheres above a certain temperature.^{39,40} This well-known morphological instability is often called Rayleigh or Plateau-Rayleigh instability and has been the subject of many investigations since its first study in the nineteenth century.^{41,42} Due to the major role played by metallic and semi-conductor nanowires in nanoelectronics and optoelectronics,¹ the morphological Rayleigh instabilities of these materials have been investigated in the past. Studies of the role of wire diameter, temperature and annealing on the nanowire morphology evolution have already been reported.^{39,40,43} The physical origin of the Rayleigh instability is also the reduction of the surface energy. If one considers a liquid cylinder with initial radius r and a sinusoidal perturbation along its axis, *i.e.*

$$r(x) = r_0(\varepsilon) + \varepsilon \cdot \sin\left(\frac{2\pi x}{\lambda}\right) \quad (4)$$

simple calculations show that the perturbations with wavelength $\lambda > 2\pi r_0$ will increase spontaneously in amplitude and thus lead to a fragmentation of the initial cylinder.⁴⁴ In reality, the morphological instabilities of a solid wire are slightly more complicated but the overall trend that is experimentally observed still remains the same.^{15,16,45} For instance the average distance between Ag nanoparticles in Figure 1e is about 750 nm, a value larger but of the same order of magnitude as $2\pi R$ (330 nm) (the difference stemming from the substrate influence, the fivefold twin structure of the wire as well coalescence which occurs after spheroidization). The Rayleigh criterion ($\lambda > 2\pi r_0$) is valid for all wire sizes, but since nanowires exhibit much higher surface to volume ratio the associated kinetics are much faster for nanowires with small

diameters. The origin of this diameter-dependent kinetics stems from the dependence of the Rayleigh instability on surface diffusion. Smaller diameter wires have a higher ratio of surface to volume and a lower total volume. This means less atoms are required to move before spheroidization occurs and a higher proportion of the atoms are moving at a given time. This morphological instability leads to a loss of the percolation character of the network and hence a sharp increase of the electrical resistance at high temperature as observed in Figure 1 and 4. **Figure 5** demonstrates that the diameter of the wires is an important factor for the onset of the Rayleigh instability, as the wire diameter decreases so does the temperature of spheroidization.

Knowing that in order to improve the electro-optical properties of AgNW networks, NWs with small diameter and large aspect ratio are often preferred,³ underlines the significance of the Rayleigh instability which becomes more of a limitation when the NW diameter decreases.

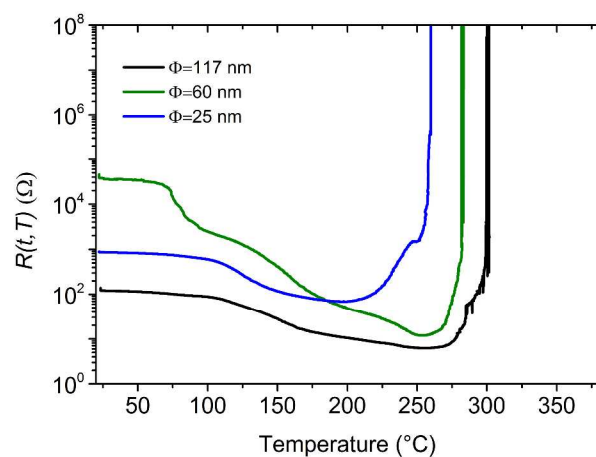


Figure 5: The impact of diameter on the response of AgNW networks to temperature when thermal ramps are used from room temperature at a rate of 2 °C per minute. The three AgNW networks have similar areal mass density of ≈ 50 mg/m².

Finally a rather direct comparison can be outlined between the present work and the investigation of Chou *et al.*³⁸ who studied the thermal effects on the properties of a film composed of Ag nanoparticles (also surrounded by a PVP layer). In both studies, in spite of the large difference in the morphology of the Ag nanostructures, the electrical resistance of the network exhibits a minimum versus the annealing temperature. In the study of Chou and co-authors, sintering and/or desorption of PVP lead to a decrease of $R(t, T)$ at low temperatures 50-200 °C, while above 200-250 °C (depending on the nanoparticle size), $R(t, T)$ increased and the networks lose their conductive properties above 400 °C due to the growth of both Ag particles and pores and the eventual breakdown of conduction pathways. These observations on spherical nanoparticles by Chou *et al.* are partially analogous to the thermal behavior presented here for Ag nanowires.

3. Conclusions

This work demonstrates that thermal annealing can drastically lower the electrical resistance of AgNW network post deposition. The electrical resistance of the networks exhibit a minimum for an annealing temperature spanning from 200 to 320 °C. Four physical mechanisms have been identified at the origin of this resistance variation with temperature: desorption of organic residues, desorption/degradation of PVP, local sintering and Rayleigh instability of the NWs. All these mechanisms were discussed and their effects described. Such an investigation enables the determination of the thermal treatment required to produce the minimum electrical resistance for a given NW density.

Annealing an AgNW network fabricated with wires of 105 nm in diameter and 37.5 μm in length at 200 °C for 2 hours results in a reduction in the sheet resistance from approximately $10^7 \Omega/\square$ to $9.5 \Omega/\square$ associated with an optical transmission of 90% at 550 nm (once the substrate transmission is removed) resulting in state-of-the-art transparent electrodes.²² Moreover sudden drops of the networks' electrical resistance were observed and interpreted as the creation of efficient percolating pathways through the network. A simple model was proposed and describes well the experimental observations. Based on the results of the present research, there are two important directions that future investigations should focus on. In order to improve the thermal stability of nanowires, embedding them within a thin oxide layer could provide an efficient method to prevent morphological instabilities. This idea has already been considered with thin transparent oxide films (ZnO or TiO₂) for which slightly higher thermal stability was achieved.²⁵ Finally the quantitative estimation of the different kinetics involved for each physical mechanism would enable better separation of their relative influences and would help calculating their importance during thermal annealing. This could yield an efficient way to foresee the evolution of the morphological and electrical properties of metallic NW networks as induced by thermal annealing and allow further optimization of the physical properties of metallic NW networks.

4. Experimental section

AgNWs (Ag115, Ag60 and Ag25 in isopropanol) were purchased from SeaShell Technology.⁴⁶ These nanowires were obtained from the polyol process^{32,47,48} for which NWs are grown in solution and are stabilized by polyvinylpyrrolidone (PVP). The nanowires are crystalline and present the five fold twinned structure typical for silver nanowires produced by the polyol method.^{28,49} This solution was then diluted with isopropyl alcohol (IPA) to various concentrations.

Substrates used were Corning C1737-S111, alkaline earth borosilicate glass, typical RMS roughness as measured by AFM was 3.4 nm with a maximum RMS roughness of 4 nm. Before spin coating the AgNW solution the substrates were cleaned by sonication in acetone for 5 minutes followed by boiling in Isopropanol for 15 minutes and then drying with nitrogen.

Deposition was performed at room temperature by spin-coating at 1500 rpm as follows: 1 mL of solution was introduced onto the rotating substrate (25 mm x 25 mm corning glass, Corning 1737) in a drop-wise manner of two stages (0.5 mL each) with a 30sec pause between each deposition. The sample was maintained at a constant rotation throughout the deposition. This produces random networks of AgNWs on glass substrates. Square specimens of 12 mm x 12 mm were cut from the larger substrates and Ag paint electrodes were deposited on two opposite edges of the network for *in-situ* measurement of the electrical resistance of the AgNW network during thermal annealing. This was performed with a two-point probe system where the electrical resistance was recorded using a Keithley sourcemeter (model 2400). Temperature is PID-controlled and recorded via two thermocouples mounted inside the heating stage and on the surface on which the sample rests, respectively.

Structural observations of the AgNWs were performed using a field-emission scanning electron microscopy (FESEM) ZEISS Ultra Plus microscope using an accelerating voltage of 10 kV. Any annealing or pre-annealing was performed in air.

5. Acknowledgements

This work has been supported by the Agence Nationale de la Recherche (Programme Matériaux et Procédés) through the project FICHTRE and by the project SEI from Grenoble INP. This work was also supported by the EACEA Erasmus Mundus funding program through IDS-FunMats. The authors would like to warmly thank J.P. Simonato, C. Celle, and C. Mayousse for fruitful discussions as well as M. Anikin and M. Jouvert for their assistance during experimental measurements.

6. References

1. J. Ji, Z. Zhou, X. Yang, W. Zhang, S. Sang, and P. Li, *Small*, 2013, **9**, 3014–3029.
2. S. De, P. J. King, P. E. Lyons, U. Khan, and J. N. Coleman, *ACS Nano*, 2010, **4**, 7064–7072.
3. S. Sorel, P. E. Lyons, S. De, J. C. Dickerson, and J. N. Coleman, *Nanotechnology*, 2012, **23**, 185201.
4. T. Tokuno, M. Nogi, M. Karakawa, J. Jiu, T. T. Nge, Y. Aso, and K. Sukanuma, *Nano Research*, 2011, **4**, 1215–1222.
5. E. C. Garnett, W. Cai, J. J. Cha, F. Mahmood, S. T. Connor, M. Greyson Christoforo, Y. Cui, M. D. McGehee, and M. L. Brongersma, *Nature Materials*, 2012, **11**, 241–249.
6. J. Lee, P. Lee, H. Lee, D. Lee, S. S. Lee, and S. H. Ko, *Nanoscale*, 2012, **4**, 6408–6414.
7. S. Han, S. Hong, J. Ham, J. Yeo, J. Lee, B. Kang, P. Lee, J. Kwon, S. S. Lee, M.-Y. Yang, and S. H. Ko, *Adv. Mater.*, 2014, **26**, 5808–5814.
8. J.-Y. Lee, S. T. Connor, Y. Cui, and P. Peumans, *Nano Lett.*, 2008, **8**, 689–692.
9. L. Hu, H. S. Kim, J.-Y. Lee, P. Peumans, and Y. Cui, *ACS Nano*, 2010, **4**, 2955–2963.
10. S. B. Sepulveda-Mora and S. G. Cloutier, *Journal of Nanomaterials*, 2012, **2012**, 7.
11. G. Guisti, D. P. Langley, M. Lagrange, R. Collins, C. Jiménez, Y. Bréchet, and D. Bellet, *International Journal of Nanotechnology*, 2014, **11**, 785–795.

12. J. H. Lee, P. Lee, D. Lee, S. S. Lee, and S. H. Ko, *Crystal Growth & Design*, 2012, **12**, 5598–5605.
13. S. De, T. M. Higgins, P. E. Lyons, E. M. Doherty, P. N. Nirmalraj, W. J. Blau, J. J. Boland, and J. N. Coleman, *ACS Nano*, 2009, **3**, 1767–1774.
14. S. Coskun, E. Selen Ates, and H. Emrah Unalan, *Nanotechnology*, 2013, **24**, 125202.
15. H. S. Shin, J. Yu, and J. Y. Song, *Applied Physics Letters*, 2007, **91**, 173106–173108.
16. H. Li, J. M. Biser, J. T. Perkins, S. Dutta, R. P. Vinci, and H. M. Chan, *Journal of Applied Physics*, 2008, **103**, 024315–024323.
17. H. Wong, *Journal of Applied Physics*, 2012, **111**, 103509–103517.
18. A. Kim, Y. Won, K. Woo, C.-H. Kim, and J. Moon, *ACS Nano*, 2013, **7**, 1081–1091.
19. L. Kavan, M. Grätzel, J. Rathouský, and A. Zukal, *J. Electrochem. Soc.*, 1996, **143**, 394–400.
20. C.-C. Yang, H. Q. Zhang, and Y. R. Zheng, *Current Applied Physics*, 2011, **11**, S147–S153.
21. H. H. Khaligh and I. A. Goldthorpe, *Nanoscale research letters*, 2013, **8**, 1–6.
22. D. Langley, G. Giusti, C. Mayousse, C. Celle, D. Bellet, and J.-P. Simonato, *Nanotechnology*, 2013, **24**, 452001.
23. V. Scardaci, R. Coull, P. E. Lyons, D. Rickard, and J. N. Coleman, *Small*, 2011, **7**, 2621–2628.
24. J.-W. Lim, D.-Y. Cho, K. Eun, S.-H. Choa, S.-I. Na, J. Kim, and H.-K. Kim, *Solar Energy Materials and Solar Cells*, 2012, **105**, 69–76.
25. F. S. F. Morgenstern, D. Kabra, S. Massip, T. J. K. Brenner, P. E. Lyons, J. N. Coleman, and R. H. Friend, *Applied Physics Letters*, 2011, **4**, 183307–183307–3.
26. J. Ajuria, I. Ugarte, W. Cambarau, I. Etxebarria, R. Tena-Zaera, and R. Pacios, *Solar Energy Materials and Solar Cells*, 2012, **102**, 148–152.
27. J. Liang, L. Li, X. Niu, Z. Yu, and Q. Pei, *Nature Photonics*, 2013, **7**, 817–824.
28. P. Lee, J. Lee, H. Lee, J. Yeo, S. Hong, K. H. Nam, D. Lee, S. S. Lee, and S. H. Ko, *Advanced Materials*, 2012, **24**, 3326–3332.
29. C. Celle, C. Mayousse, E. Moreau, H. Basti, A. Carella, and J.-P. Simonato, *Nano Research*, 2012, **5**, 427–433.
30. S. Sorel, D. Bellet, and J. N. Coleman, *ACS Nano*, 2014, **8**, 4805–4814.
31. H. Ibach, *Physics of surfaces and interfaces*, Springer, Berlin; New York, 2006.
32. Y. Sun, B. Mayers, T. Herricks, and Y. Xia, *Nano Lett.*, 2003, **3**, 955–960.
33. A. Bid, A. Bora, and A. K. Raychaudhuri, *Phys. Rev. B*, 2006, **74**, 035426–035426–8.
34. D. R. Lide, *CRC Handbook of Chemistry and Physics 2004-2005: A Ready-Reference Book of Chemical and Physical Data*, CRC press, 2004.
35. A. Mayoral, L. F. Allard, D. Ferrer, R. Esparza, and M. Jose-Yacamán, *J. Mater. Chem.*, 2010, **21**, 893–898.
36. R. M. German, *Sintering Theory and Practice*, Wiley, 1996.
37. A. Vagnon, O. Lame, D. Bouvard, M. D. Michiel, D. Bellet, and G. Kapelski, *Acta Materialia*, 2006, **54**, 513–522.
38. K.-S. Chou, K.-C. Huang, and H.-H. Lee, *Nanotechnology*, 2005, **16**, 779–784.
39. M. E. Toimil Molaes, A. G. Balogh, T. W. Cornelius, R. Neumann, and C. Trautmann, *Applied Physics Letters*, 2004, **85**, 5337–5339.
40. S. Karim, M. E. Toimil-Molaes, A. G. Balogh, W. Ensinger, T. W. Cornelius, E. U. Khan, and R. Neumann, *Nanotechnology*, 2006, **17**, 5954–5959.
41. J. Plateau, *Translated Annual Reports of the Smithsonian Institution*, 1873, 1863.
42. L. Rayleigh, *Proceedings of the London Mathematical Society*, 1878, **s1-10**, 4–13.
43. C.-P. Hsiung, H.-W. Liao, J.-Y. Gan, T.-B. Wu, J.-C. Hwang, F. Chen, and M.-J. Tsai, *ACS Nano*, 2010, **4**, 5414–5420.
44. P.-G. de Gennes, F. Brochard-Wyart, and D. Quéré, *Capillarity and Wetting Phenomena - Drops, Bubbles, Pearls, Waves*, Springer New York, 2004.
45. J. P. Naik, K. Das, P. D. Prewett, A. K. Raychaudhuri, and Y. Chen, *Applied Physics Letters*, 2012, **101**, 163108.
46. <http://www.seashelltech.com/index.shtml>, <http://www.seashelltech.com/index.shtml>.
47. Y. Sun, B. Gates, B. Mayers, and Y. Xia, *Nano Lett.*, 2002, **2**, 165–168.
48. Y. Sun and Y. Xia, *Advanced Materials*, 2002, **14**, 833–837.
49. Y. Sun, Y. Ren, Y. Liu, J. Wen, J. S. Okasinski, and D. J. Miller, *Nature Communications*, 2012, **3**, 971.